Journal of CO2 Utilization 78 (2023) 102621

Contents lists available at ScienceDirect

Journal of CO2 Utilization

journal homepage: www.elsevier.com/locate/jcou

Noble metal nanoparticles and nanodiamond modified strontium titanate photocatalysts for room temperature CO production from direct hydrogenation of CO_2

Mohit Yadav [a], Tamás Gyulavári [a], Janos Kiss [a], Kornélia B. Ábrahámné [a], Anastasiia Efremova [a], Ákos Szamosvölgyi [a], Zsolt Pap [a,b,c,*], András Sápi [a,**], Ákos Kukovecz [a], Zoltán Kónya [a,d]

[a] Department of Applied and Environmental Chemistry, Interdisciplinary Excellence Centre, University of Szeged, H-6720, Rerrich Béla Sqr. 1, Szeged, Hungary
[b] Nanostructured Materials and Bio-Nano-Interfaces Center, Interdisciplinary Research Institute on Bio-Nano-Sciences, Babes-Bolyai University, Treboniu Laurian 42, RO-400271 Cluj-Napoca, Romania
[c] Institute of Research-Development-Innovation in Applied Natural Sciences, Babes-Bolyai University, Fântânele Str. 30, RO-400294 Cluj-Napoca, Romania
[d] ELKH-SZTE Reaction Kinetics and Surface Chemistry Research Group, University of Szeged, Rerrich Béla tér 1, Szeged 6720, Hungary

ARTICLE INFO

Keywords:
Strontium titanate
Noble metals
Nanodiamonds
Carbon dioxide
Photocatalysis

ABSTRACT

The activation and conversion of CO_2 can be achieved on multifunctional catalytic sites at the metal/oxide interface by taking advantage of the synergy between noble metal nanoparticles and supports. Herein, sequential deposition of noble metals (Ru, Rh, and Pt) and nanodiamonds (NDs) was carried out on the surface of strontium titanates (STO). The noble metals and NDs were deposited in either 1 wt% or 10 wt%. The samples were characterized with in-situ as well as ex-situ spectroscopic and microscopic techniques and tested towards photocatalytic CO_2 hydrogenation. The sequential deposition of the noble metals and NDs enhanced light absorption properties, which also led to higher photocatalytic activity. The STO-ND-Ru sample had the highest photocatalytic CO_2 hydrogenation efficiency (47.5%) and showed improved selectivity for CH_4 (14.5%). Diffuse reflectance infrared Fourier transform spectroscopy (DRIFTS) studies showed that the hydrogenation of CO_2 to CO and CH_4 followed different mechanisms for pristine STO and STO-ND-Ru.

1. Introduction

Over the past few decades, one of the most pressing concerns has been to minimize the ever-increasing CO_2 emissions that cause global warming and climate change. Consequently, various catalytic technologies have been successfully implemented to transform CO_2 into useful hydrocarbons, such as electrochemical [1–3] and heterogeneous [4–6] catalysis. One of the techniques that is of particular interest is photocatalysis. It only requires the harnessing of sunlight as an energy source, and it can mimic natural photosynthesis at room temperature [7,8]. However, the realization of photocatalytic CO_2 reduction on an industrial scale has not yet been achieved, which requires further search for a novel and efficient photocatalyst [9]. Recently, perovskite oxides have gained tremendous interest in a broad range of reactions owing to their unique structural flexibility [10]. These oxides also possess band edges that can be tuned and modified to facilitate CO_2 reduction. In particular, titanate perovskites have shown promising photocatalytic reduction potential owing to their excellent photochemical stability [11–13].

Strontium titanate (STO) is a typical perovskite-type multi-metal oxide and a potential photocatalyst, which might be particularly suitable for the photocatalytic reduction of CO_2. This is because it has high chemical and thermal stability, and a more negative conduction band edge in comparison to TiO_2 (by ~200 mV) [14]. Also, pristine STO possesses an indirect band gap of ~3.2 eV, which means that UV light is required to activate it [15–17]. Moreover, due to the poor quantum efficiency and fast recombination of photoinduced charges, the performance of STO is limited [18]. Therefore, it is imperative to prolong the separation of photogenerated electrons (e^-) and holes (h^+) to enhance its performance in photocatalytic CO_2 reduction [19]. In this regard, numerous approaches have been proposed including structural

* Corresponding author at: Department of Applied and Environmental Chemistry, Interdisciplinary Excellence Centre, University of Szeged, H-6720, Rerrich Béla Sqr. 1, Szeged, Hungary.
** Corresponding author.
E-mail addresses: pzsolt@chem.u-szeged.hu (Z. Pap), sapia@chem.u-szeged.hu (A. Sápi).

https://doi.org/10.1016/j.jcou.2023.102621
Received 6 July 2023; Received in revised form 20 October 2023; Accepted 8 November 2023
Available online 22 November 2023

engineering, shape control, increasing the number of oxygen vacancies, doping, coupling with other perovskite or metal oxides and so on. For example, STO has been coupled with $SrTiO_3$/CuO [20], $SrTiO_3/SnNb_2O_6$ [21], $SrTiO_3/LaTiO_3$ [22] to establish a heterojunction for suppressing the recombination of e^-h^+ pairs. Modifying STO with nanosized noble metals and carbon-based nanoparticles (such as nanodiamonds) is another effective strategy to reach this goal. This is because incorporating them can result in the development of surface plasmon resonance (SPR) and heterojunction, which can boost the reduction potential of STO [23–26]. For example, Mateo et al. reported the design of RuO_2 nanoparticles supported on STO, which showed excellent photocatalytic activity towards CO_2 methanation. They managed to reach close to 50% efficiency in a continuous flow setting under visible light irradiation [27]. In another publication, a Pt/STO photocatalyst was successfully applied for water splitting without any side reactions. The Pt nanoclusters remained oxidized on the surface of STO and were resistant to CO poisoning during the reaction [28]. Wu and coworkers synthesized Rh-doped and undoped STO photocatalysts via a polymerizable complex method and a hydrothermal method. They achieved high photocatalytic activity towards both CO_2 reduction and H_2 evolution under visible light irradiation [29]. Shoji et al. reported the development of a rhodium-modified STO, which was used for reforming methane at low temperatures (without heat supply) under UV light irradiation. It was observed that doping STO with Rh can utilize the energy of photons to achieve valuable products from different carbon resources [30].

Nanodiamonds (NDs), a form of carbon, possess excellent catalytic properties because of their unique crystalline structure comprising of sp2 hybrid graphite and a sp3 diamond core. NDs have small particle size (typically between 4 and 5 nm) and large specific surface area ($\sim$300 $m^2 \cdot g^{-1}$), which makes them suitable for photocatalytic applications [26]. There are various reports on coupling NDs with metal oxides such as TiO_2 [31], ZnO [32], and Cu_2O [33]. This resulted in the formation of a heterojunction that enhanced charge transfer, charge separation, and consequently, photocatalytic activity. However, there are hardly any reports in the literature showing the association of NDs with STO along with noble metals for photocatalytic CO_2 reduction.

In this study, we demonstrate the modification of STO with noble-metals (Pt, Rh, and Ru) and nanodiamonds (NDs) to develop a novel photocatalytic scheme. Noble metals were used to utilize their SPR phenomenon, manifesting their effect as a light sensitizer as well as a photoelectron accumulator. The addition of NDs can serve as a heterojunction with STO for better charge separation and transfer. Therefore, the main aim of this work was to investigate the sequential deposition of noble metals and NDs on STO in various weight ratios. The present approach could be an asset in the design and development of highly efficient ternary composites for photocatalytic CO_2 reduction.

2. Experimental

2.1. Materials

Strontium nitrate (Molar Chemicals, 98.5%) and titanium(IV) butoxide (Sigma-Aldrich, reagent grade, 97%) were used as $SrTiO_3$ precursors. Potassium hydroxide (KOH, VWR Chemicals, Ph. Eur. grade) was used to set an alkaline environment. Ruthenium(III) chloride (Sigma-Aldrich), rhodium(III) chloride (Sigma-Aldrich), and chloroplatinic acid hexahydrate (Sigma-Aldrich) were used as precursors for the synthesis of Ru, Rh, and Pt nanoparticles. Nanodiamond powder ($<$ 10 nm, $\geq$97% Sigma-Aldrich) was purchased from Merck, Hungary. Ethanol (Molar Chemicals, absolute ethanol) and Milli-Q water were used to purify the samples via centrifugation. A gas mixture of CO_2:H_2 = 1:2 ratios was used for the photocatalytic activity measurements. Commercial $SrTiO_3$ (Alfa Aesar, 99%) was used as a reference photocatalyst.

2.2. Synthesis

The synthesis procedure was based on the publication of Jiang et al. [34]. In a typical procedure, 3.96 g of $Sr(NO_3)_2$ was dissolved in 30 mL of Milli-Q water under continuous stirring. In a separate beaker, 60.59 g (1.08 mol) of KOH powder was slowly dissolved in 60 mL of Milli-Q water. After the latter solution cooled down, 15 mmol of Aeroxide P25 (1.2 g) was added. Subsequently, the $Sr(NO_3)_2$ solution and P25/KOH solution were mixed together and stirred for another 1 h. Afterwards, the resulting mixture was transferred into a 150 mL stainless-steel Teflon--lined autoclave and placed in an oven at 180 °C for 12 h. After cooling down to room temperature naturally, the material was collected and washed via centrifugation with Milli-Q water and ethanol several times. After drying at 80 °C in air, the sample (4 $g \cdot L^{-1}$) was put in a 0.01 M HCl solution for 2 h, washed via centrifugation the same way as in the previous step, and dried overnight in an oven at 80 °C.

The modification of STO with noble metals (hereinafter referred to as STO-X, where X = Ru, Rh, or Pt) was based on the publication of Wang et al. [35]. STO (250 mg) was added to 50 mL of Milli-Q water, followed by ultrasonication for 20 min. Then, the solution of either Ru, Rh or Pt (1 wt%) was added dropwise to the STO suspension followed by stirring for 4 h at 50 °C. The samples were washed with Milli-Q water and ethanol for several times and dried overnight at 80 °C in air. The samples containing both noble metals and NDs (STO-X-ND and STO-ND-X) were synthesized similarly, by using an STO sample as starting material that already contained the given component. The order of components in the sample names corresponds with the order in which the components were added during preparation.

2.3. Characterization

X-ray diffraction (XRD) patterns were recorded using a Rigaku Miniflex-II X-ray diffractometer with Ni-filtered Cu Kα radiation (λ = 1.54 Å) operated at 30 kV and 15 mA. X-ray photoelectron spectroscopy (XPS) spectra were obtained on a Specs instrument equipped with an XR50 dual anode X-ray source and a Phoibos 150 hemispherical electron analyzer. The Al Kα X-ray source was operated at 150 W (14 kV). Survey spectra were collected at 40 eV pass energy with a step rate of 1 eV. High-resolution spectra were collected at a pass energy of 20 eV with an energy resolution of 0.1 eV. All high-resolution spectra were charge corrected for the aliphatic component of the C1s spectrum region (peak maximum at 284.8 eV). For background correction, a standard Shirley background was applied in all cases. The morphological characterization of each sample was carried out with a FEI TECNAI G2 20 X-Twin high-resolution transmission electron microscope (TEM). Raman spectra were measured on a Bruker Senterra II Raman microscope using a 785 nm laser with a nominal power of 100 mW. The integration time was 10 s and each spectrum was generated by the software based on 10 scans. Diffuse reflectance infrared Fourier transform spectroscopy (DRIFTS) analyses were carried out with an Agilent Cary-670 FTIR spectrometer equipped with a Harrick Praying Mantis™ diffuse reflectance attachment. The sample holder contained two BaF_2 windows in the infrared path. The samples were pretreated as described below in Section 2.4, cooled down to room temperature under helium flow, then, the background spectrum was recorded. At room temperature, a CO_2:H_2 mixture (1:2) with a total flow rate of 15 $mL \cdot min^{-1}$ were fed into the DRIFTS cell followed by UV irradiation for 1, 5, 10, and 20 min. The tubes were externally heated to avoid condensation. All spectra were recorded between 4000 and 900 cm^{-1} at a resolution of 2 cm^{-1}. Typically, 32 scans were taken. Due to the short optical path within the DRIFTS cell, the contribution of the reactant gases was negligibly small.

2.4. Photocatalytic CO_2 hydrogenation performance

Photocatalytic CO_2 hydrogenation measurements were performed in a flow microreactor that comprised of an outer glass cylinder (dimension

= 10.2 cm, h = 25 cm) and an inner glass cylinder (dimension = 6.4 cm, h = 25 cm). The inner glass cylinder contained a 500 W mercury vapor lamp (Heraeus Noblelight TQ 718, Hanau, Germany; λ_{max} = 254 nm) as a light source that was operated under constant water cooling. The irradiation intensity of the 500 W mercury vapor lamp on the photocatalytic surface was measured with a Quantum meter (Apogee, Model MQ-200), and it was observed to be 1083 μmol m^{-2} s^{-1}. First, 250 mg of catalyst was ultrasonically suspended in 10 mL of absolute ethanol, followed by immobilization on the outer surface of the inner glass cylinder. Second, the immobilized catalysts were pretreated at 250 °C with a heating rod, and various gases were introduced into the space between the cylinders (Ar for 20 min, O_2 for 30 min, Ar for 10 min, and H_2 for 60 min). Third, the reactant gas mixture (CO_2:H_2 at a ratio of 1:2) was introduced into the space between the cylinders with an Aalborg mass flow controller. A pump was used to recirculate the fixed amount of reactant gas mixture between the gas chromatograph (GC) and the reactor. During the measurements, a constant (room) temperature was set by recirculating cooling water through the system. Fourth, the separation of the products and the reactants were carried out in a HP 5890 Series II GC equipped with a 2-meter-long (d = 0.635 cm) capillary column packed with a Porapak QS polymer. The gases were detected with a flame ionization detector and thermal conductivity detector.

3. Results and discussion

3.1. Characterization

The powder XRD patterns of STO, STO-X, STO-X-ND and STO-ND-X composites are presented in Fig. 1. For pristine STO nanoparticles, the characteristic diffraction peaks at 22.55°, 32.28°, 39.81°, 46.48°, 57.56°, and 67.61° can be attributed to the (100), (110), (111), (200), (211) and (220) planes of cubic STO (PDF#35–0734), respectively [34]. Pure NDs (Fig. S1) show two characteristic diffraction peaks at 43.24° and 75.92° corresponding to the (220) and (310) planes. Primary crystallite sizes were calculated via the Scherrer formula, and the results are shown in Table 1. The sizes of the noble metal- and NDs containing samples remained almost the same in comparison with that of the STO sample. Moreover, the XRD patterns of STO-X-ND and STO-ND-X composites also remained almost identical to pristine STO, showing that ND deposition even at 10 wt% did not cause any structural change in STO.

The optical properties of the pristine STO, ND, STO-X, STO-X-ND, and STO-ND-X samples were investigated by DRS and the results are shown in Fig. 2**a**. It could be observed that all the absorption spectra

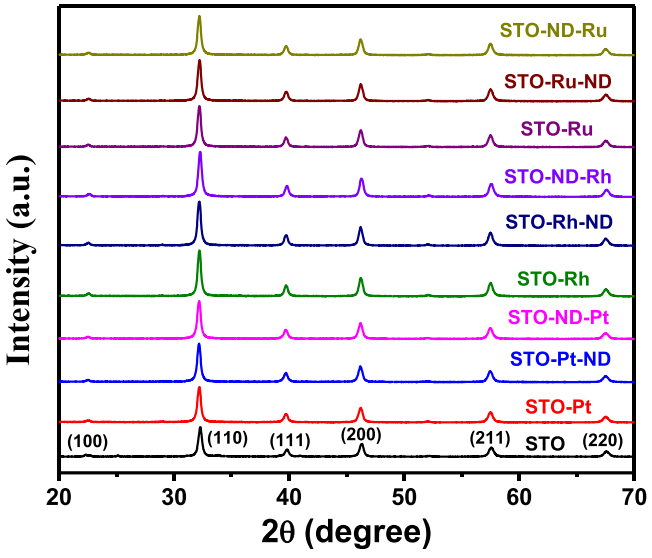

Fig. 1. XRD patterns of STO and STO-based composites.

Table 1
Catalyst loadings, BET surface areas, band gaps and primary crystallite size values.

Sample	Rh, Ru and Pt (wt %)	ND (wt %)	SSAs ($m^2 \cdot g^{-1}$)	Band gap (eV)	Primary crystallite size (nm)
STO	-	-	51.8	3.28	19.3
ND	-	-	302.5	2.88	3.59
STO-Pt	1	-	52.7	3.24	19.53
STO-Pt-ND	1	10	71.8	3.22	20.7
STO-ND-Pt	1	10	72.1	3.16	20.78
STO-Rh	1	-	53.7	3.26	19.34
STO-Rh-ND	1	10	70.7	3.25	20.24
STO-ND-Rh	1	10	72.3	3.17	20.4
STO-Ru	1	-	52.9	3.23	19.31
STO-Ru-ND	1	10	70.9	3.2	19.98
STO-ND-Ru	1	10	73.8	3.08	20.23

exhibited the typical behavior of wide band gap oxide semiconductors, having an intense absorption band with a steep edge. Pristine STO showed high absorption at wavelengths shorter than 400 nm, which could be assigned to its intrinsic band gap absorption. Compared with that of pristine STO, the absorption of STO-based composites presented a slight redshift in light response. The absorption intensities of the STO-X samples were almost the same in the UV light range. This was expected because the synthesis method employed resulted in the deposition of noble metal NPs on the surface of STO, but not in their incorporation into the STO lattice. The addition of NDs resulted in both a redshift and the increase of absorption in the visible light range, which was more pronounced for the STO-ND-X samples. The first-order transmittance spectra were derived and the x positions of the peak maxima were used to determine the band gaps (Table 1) [36]. Overall, the order of noble metal- and ND-additions influenced the band gaps. The STO-ND-X samples possessed lower band gaps than the STO-X-ND samples, as the noble metals were widely available when added as the last components. However, the addition of NDs as the last component might have covered up noble metals decreasing the changes in optical properties and photocatalytic activity. Similarly, to our findings on primary crystallite size, no notable trend could be observed in the change of SSAs for the STO-X samples (Table 1). As expected, the NDs with large SSA resulted in increased SSAs for the STO-X-ND and STO-ND-X sample series. Raman spectroscopy measurements were carried out to study the vibrational modes and structural phase transitions in the STO, STO-Ru, STO-Rh and STO-Pt samples (Fig. 2**b**). For the pristine STO, all first-order Raman lines are symmetry forbidden. The optical phonons observed correspond to the positions of first-order transverse and longitudinal lines, that is, $TO_2 + LO_1$, TO_4, and LO_4 of pure stoichiometric STO lattice [37]. The strong scattering at low frequency (116 cm^{-1}) likely arises from the same phenomenon due to the activation of the soft mode TO_1. According to lattice dynamics calculations, the $TO_2 + LO_1$ phonon corresponds to the vibration of Sr ions against the TiO_6 octahedra, while $TO_3 + LO_2$ corresponds to O–Sr–O bending vibrations. The TO_3 and LO_4 phonons located at 542 cm^{-1} and 801 cm^{-1} can be attributed to Ti–O–Ti bending and Ti–O stretching vibrations, respectively [38]. For the STO-X samples, similar peak positions were observed as for the pristine STO. However, the peak intensities of first- and second-order Raman scatterings in STO-Ru, STO-Rh and STO-Pt were lower significantly, indicating that the cubic structure of STO was weakened [39].

TEM measurements were carried out to investigate morphology and the presence of noble metals and NDs on the surface of STO (Fig. 3). The TEM micrograph of pure STO exhibit cubic-like morphology with an average diameter of about 40–60 nm (Fig. 3**a**). The Ru, Pt, and Rh

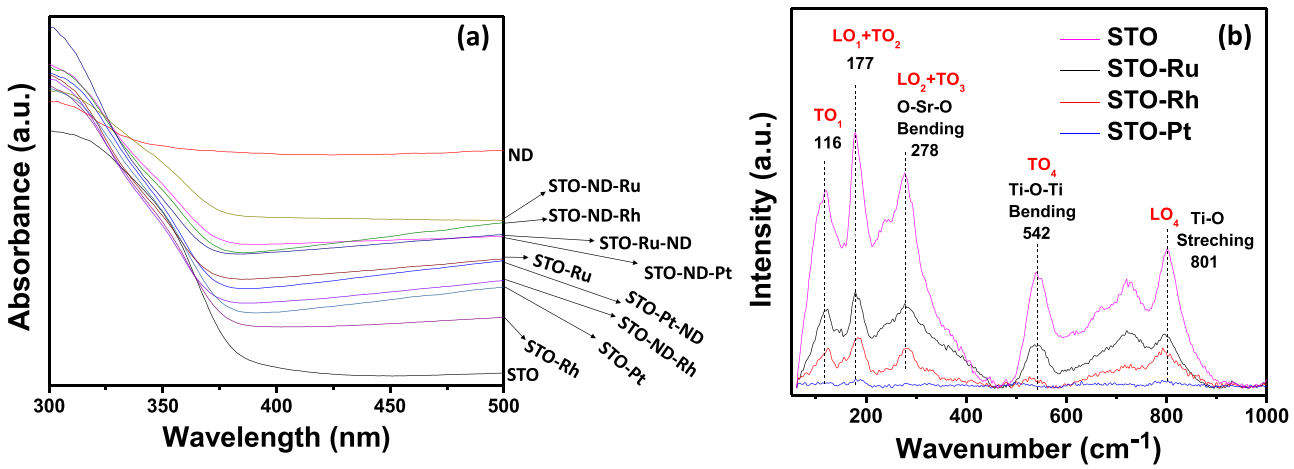

Fig. 2. (a) Diffuse reflectance spectra of pristine STO, ND, STO-X, STO-X-ND and STO-ND-X composites; (b) Raman spectra of STO, STO-Ru, STO-Rh, and STO-Pt samples.

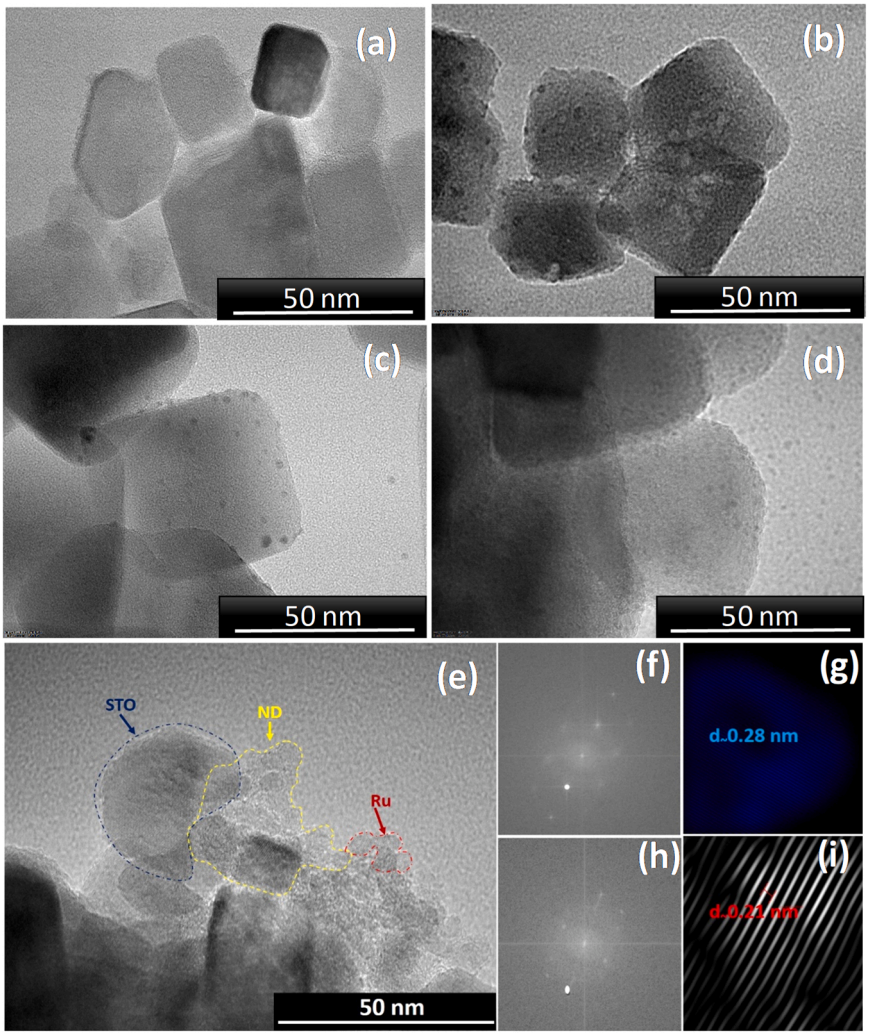

Fig. 3. TEM micrographs of (a) STO, (b) STO-Ru, (c) STO-Pt, (d) STO-Rh, (e) STO-ND-Ru samples. (f and h) FFT patterns for STO and Ru. (g and i) Inverse FFT patterns for STO and Ru.

nanoparticles have an average diameter of 1–2 nm, while the NDs are made up of cubic-like particles of different sizes forming agglomerates (Fig. S2a–**d**). For STO-Ru, STO-Rh, and STO-Pt, the noble metals seem to be uniformly deposited on the surface of STO, which can further be evidenced by the EDX results (Fig. S2e–**g**). The TEM micrograph of STO-ND-Ru showed that the surface of STO was considerably covered with NDs (yellow dotted region) and Ru nanoparticles (in red region). The lattice spacing observed at ~0.28 nm and 0.21 nm, corresponded to the

(110) and (101) crystallographic planes of STO and Ru nanoparticles [40]. For NDs, no lattice fringes were observed because of their slightly amorphous structure. The coexistence of STO, ND, and Ru nanoparticles was confirmed by EDX measurements (Fig. S2h). The elemental maps of STO-ND-Ru (Fig. S2i–**m**) were also recorded, which confirmed that NDs and Ru were indeed present on the surface of STO in this sample.

3.2. Photocatalytic performance

In the previous section, we showed that the sequential photodeposition of noble metals and NDs influenced the light absorption and band gap of composites. This observation is the first sign that studying the "build-up" sequence of a nanocomposite is of great importance. Thus, photocatalytic CO_2 reduction experiments were performed to evaluate the difference in photoactivity that could be caused by the localization of noble metals and NDs. Initially, control experiments were conducted (Fig. S3a), and it was observed that the catalysts were inactive in the dark. However, after irradiation, pristine STO had a photoreduction activity of 35.5% for CO_2, which is almost 2.2 and 2.8 times higher than that of commercial STO (12.8%) and NDs (11.1%), respectively.

The results of CO_2 photoreduction for the STO-based composites as a function of time are presented in Fig. 4**a**. The results revealed that all photocatalysts showed a linear increase. Pt and Rh enhanced the photocatalytic activity of STO only marginally. In comparison, STO-Ru showed improved activity along with higher formation rates for CO and CH_4 (Fig. S3b). This may be attributed to the strong Schottky barrier that formed at the interface of Ru and STO, which efficiently trapped electrons and inhibited electron–hole recombination [41]. As expected, NDs in STO-ND slightly improved the photoreduction of CO_2, and they significantly enhanced the formation rate of CH_4 that was almost four times higher than that for pristine STO. Significant differences were observed between the photoactivity of STO-X-ND and STO-ND-X sample series, which confirms that the sequential deposition of noble metals and NDs is crucial. In the presence of noble metals on the surface of STO, the photocatalytic performances showed the same trend observed for STO. The only differences were the higher efficiency and higher formation rate for CO. STO-ND-X composites were significantly more active towards CO_2 photoreduction than pristine STO. STO-ND-Ru turned out to be the best photocatalyst, reaching as high as 47.5% conversion for CO_2 and the highest formation rate for both CO and CH_4. It is evident that the direct coupling of NDs with STO is effective for reaching high activity, which is also apparent in the increasing selectivity for CH_4 (Fig. S3c). It was mostly CO that was produced by all the photocatalysts; however, the ratio of CH_4 to CO improved with the addition of NDs as shown in Table 2.

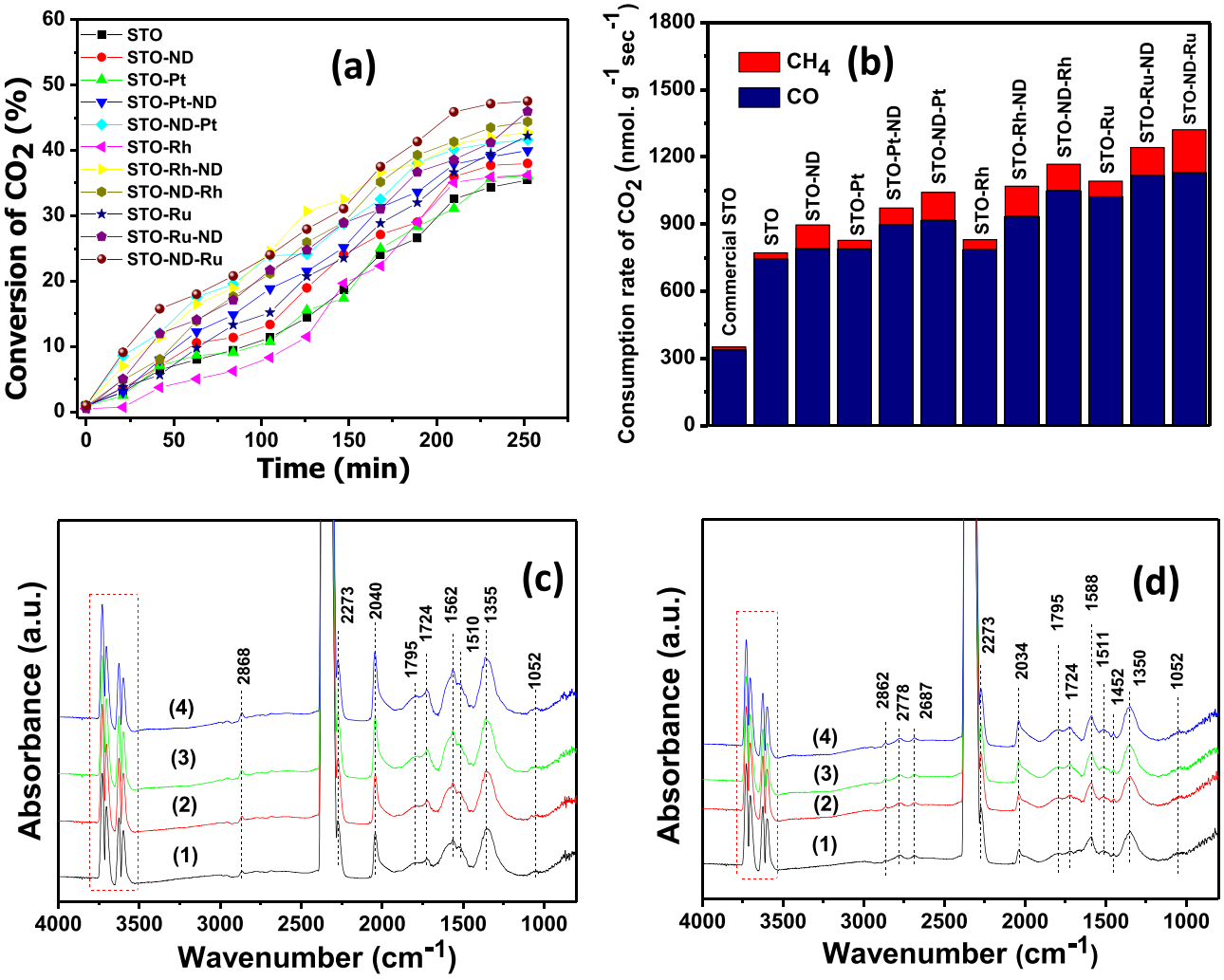

Fig. 4. (a) Conversion of CO_2 with STO and noble metal- and ND-containing samples under light irradiation. (b) consumption rate of CO_2 with STO, STO-X, STO-X-ND, and STO-ND-X composites. DRIFTS spectra of (c) STO-Ru-ND and (d) STO-ND-Ru samples. The numbers in the last three figures represent the following: (1) at room temperature for 20 min, (2) at room temperature for 20 min + under UV exposure for 5 min, (3) at room temperature for 20 min + under UV exposure for 10 min, and (4) at room temperature for 20 min + under UV exposure for 20 min.

Table 2
Conversion of CO_2, formation rate and selectivity of the products obtained with STO, STO-X, STO-X-ND and STO-ND-X photocatalysts.

Samples	CO_2 conversion (%)	Formation of products ($nmol \cdot g^{-1} \cdot sec^{-1}$)		Selectivity (%)	
		CO	CH_4	CO	CH_4
STO	35.5	744.8	27.1	96.5	3.5
STO-ND	38.1	790.5	105.4	88.2	11.8
STO-Pt	36.1	788.1	38.3	95.4	4.6
STO-Pt-ND	39.9	896.7	74.5	92.3	7.7
STO-ND-Pt	41.6	917.3	123.8	88.1	11.9
STO-Rh	36.2	786.4	43.5	94.8	5.2
STO-Rh-ND	42.8	936.1	132.2	90.1	9.9
STO-ND-Rh	44.4	1050.7	116.4	87.6	12.4
STO-Ru	42.3	1022.4	69.3	93.6	6.4
STO-Ru-ND	45.9	1117.1	124.4	89.9	10.1
STO-ND-Ru	47.5	1131.5	190.3	85.6	14.4

The deposition of noble metals and NDs has greatly promoted the photocatalytic reduction of CO_2 over STO. To understand the mechanism, we recorded the characteristic CO_2-TPD profiles of the as-optimized STO-ND-Ru sample along with pristine STO in the 100–300 °C temperature range (Fig. S4**)**. Both the samples exhibited similar profiles, which could further be deconvoluted into three desorption peaks at lower temperatures (84 °C and 93 °C), and one peak at a moderate temperature (152 °C). The intensities of the CO_2-TPD curves for STO-Ru-ND were observed to be increased along with a shift of the peak at the moderate temperature from 152 °C to 166 °C. This suggests the binding of the chemisorbed carbonate groups such as bicarbonates, bidentate carbonate, and monodentate carbonates to the surface of the catalyst [42]. Thus, the deposition of Ru and NDs played a crucial role in enhancing CO_2 adsorption by improving the adsorption and activation of CO_2 molecules, thus facilitating the reduction of CO_2. To assess the stability and reusability of the as-optimized STO-ND-Ru sample, we carried out the photocatalytic CO_2 reduction experiments three times. As shown in Fig. S5a, STO-ND-Ru sample showed great stability and largely retained (the decrease in CO_2 conversion was less than ~2% after three runs). Furthermore, the STO-ND-Ru sample was analyzed by XRD and SEM measurements after the reusability tests, and the results are shown in Fig. S5b**–d.** The results showed no major differences in the crystal structure, and the morphology remained intact, which further proves the structural stability of the sample. Moreover, the efficiency of the as-optimized STO-ND-Ru sample was compared with some of the previously reported STO-based materials towards photocatalytic CO_2 hydrogenation under different reaction conditions, which is summarized in Table 3.

To elucidate the reaction pathway of catalytic CO_2 reduction, in-situ DRIFTS characterization of pristine STO, STO-Ru-ND, and STO-ND-Ru was performed. STO was used as a reference, while STO-Ru-ND and STO-ND-Ru were selected due to their distinct photoactivity. For pristine STO (Fig. S6), two strong twin-bands bands at 3750–3550 cm^{-1} correspond to the combined tones gas and adsorbed CO_2 molecules [49]. Bands detected at 1672 cm^{-1} and 1310 cm^{-1} can be attributed to carboxylic species (*COOH), which are one of the key intermediates during the catalytic thermal and photoreduction of CO_2 to CO [50]. The bands at 1620 cm^{-1}, 1410 cm^{-1}, 1220 cm^{-1}, and 1058 cm^{-1} are adsorbed bicarbonate species. The strong band at 1517 cm^{-1} can be attributed to inorganic carboxylate [51]. The slight dissociation of carboxylate was also detected, as evidenced by the appearance of adsorbed CO at ~2080 cm^{-1}. The shoulder band between strong 1517 cm^{-1} and 1620 cm^{-1} at ~1560 cm^{-1} may be attributed to ν_a (OCO) vibration modes of bridged formate. The corresponding C–H deformations were detected at 2874 cm^{-1} [48]. It is probable that formate formed from carboxylate and bicarbonate species due to light irradiation [52]. It is important to mention that formyl-like (CH_2O) species could not be detected around 1720–1780 cm^{-1} on the metal free sample. The formation of CO and CH_4 occurred via RWGS mechanism based on the following chemical equations:

$$STO\text{-}ND\text{-}Ru\ (\geq E_{bg}) \rightarrow STO\ (h^+)\text{-}ND(e^-)\text{-}Ru \rightleftharpoons STO\ (h^+)\text{-}ND\text{-}Ru(e^-) \quad (1)$$

$$CO_2(g) \rightarrow CO_2^* \quad (2)$$

$$CO_2^* + Ru(e^-) + H \rightarrow COOH^* \quad (3)$$

$$COOH^* + Ru(e^-) + H \rightarrow CO^* + H_2O \quad (4a)$$

$$CO^* \rightarrow CO \quad (4b)$$

$$CO^* + H_2O + H \rightarrow {}^*HCO \quad (5)$$

$$^*HCO + H \rightarrow {}^*CH + {}^*O \quad (6)$$

$$^*CH + {}^*O + H \rightarrow {}^*CH_2 + H_2O \quad (7)$$

$$^*CH_2 + H \rightarrow {}^*CH_3 \quad (8)$$

$$^*CH_3 + H \rightarrow {}^*CH_4 \rightarrow CH_4 \quad (9)$$

$$CO_{2(a)}^* + H_{(a)}\ (OH_{(a)}) \rightarrow (HCO_3^-) + h\nu \rightarrow HCOO_{(a)} + O_{(a)} \quad (10)$$

$$STO(h^+) + H_2O \rightarrow OH^- + H^+ \quad (11)$$

$$STO(h^+) + OH^- \rightarrow OH^* \quad (12)$$

$$OH^* + {}^*CH_3 \rightarrow CH_3OH \quad (13)$$

Significant changes were observed in the case of STO-Ru-ND and STO-ND-Ru (Fig. 4**c and d**). Compared to pristine STO, slightly weak intensity peaks formate surface complex formation was observed at 1562 cm^{-1}, 1588 cm^{-1}, and 1355–1350 cm^{-1} even in thermal process at ~50^0 C. These bands are attributed to ν_a(OCO) and ν_s(OCO) vibration modes of bridged formate slightly intensified during photoinduced catalytic reduction. New intense bands appeared for both samples at 1795 cm^{-1} and 1724 cm^{-1} that were identified as formyl species (CH_2O_x) [53], resulting probably from the breakdown of formate [54]. It is clearly seen that the formate is a photoactive intermediate which was observed in other catalytic system. We suggest that for the Ru-containing catalysts, the reaction proceeds in a different way, that is, via a formate mechanism. In our present case we believe that the Ru ions may have coordinated the formate and facilitated the weakening of C═O bonds. A further photogenerated hole and a H_2 molecule constitute enough activation energy for the reduction [55,56]. Interestingly, for

Table 3
Comparison of the photocatalytic CO_2 hydrogenation performance of STO-ND-Ru sample with the previously reported samples under certain reaction conditions.

S.No.	Sample	Reaction condition	Yield of products ($nmol \cdot g^{-1} \cdot s^{-1}$)	Reference
1.	$SrTiO_3$_2	500 W mercury vapor lamp	CO (377), CH_4 (7.8)	[43]
2.	RuO_2/STO	300 W Xe lamp, 108 mW cm^{-2}, 150 °C	CO (4055)	[27]
3.	CuxO/CoPi-STO	UV light (Hg–Xe lamp)	CO (350)	[44]
4.	Cu/STO(NC)-MPS	High-pressure Hg lamp (450 W)	CO (630)	[45]
5.	Ni-STO@T	Microsolar 300 A xenon lamp, 300 W, pressure: 80–90 Kpa, 100 °C	CO (537.5), CH_4 (738.5)	[46]
6.	$SrTiO_3$ submicron cubes	300 W Xe lamp	CH_4 (439)	[47]
7.	Rh(PD)-Au@STO	300-W Xe lamp with L42 cutoff filter (λ > 400 nm) /3 mL H_2O and 70 kPa CO_2	CO (369.2), CH_4 (2.8)	[23]
8.	STO_15_SCO	Hg/Xe lamp (200 W, light intensity: 200 mW·cm^{-2}	CH_4 (40)	[48]
9.	**STO-ND-Ru**	500 W mercury vapor lamp	**CO (1131.5), CH_4 (190.3)**	**Present study**

STO-ND-Ru (Fig. 4**d**), the symmetric and asymmetric CH_2 stretches (2687 cm^{-1}, 2778 cm^{-1}, and 2862 cm^{-1}) [57] were more intense in comparison to those of STO-Ru-ND (Fig. 4**c**). This also correlates with the higher formation rate and selectivity for CH_4. Meanwhile, the intensity of linearly adsorbed CO at 2040 cm^{-1} and other carbonates was prominent for STO-Ru-ND (Fig. 4**d**), which resulted mostly in the formation of CO. This finding is in good agreement with the results of photocatalytic CO_2 hydrogenation measurements. So, the following chemical reactions may be considered:

$$HCOO^- + H^+ + h\nu \rightarrow CH_2O + O_a \quad (14)$$

$$CH_2O_a + h\nu \rightarrow CO + H_2 \quad (15)$$

$$HCOO^- + H^+ + h\nu \rightarrow CO_a + H_2O_a \quad (16)$$

$$CH_2O + H \rightarrow CH_3O \quad (17)$$

$$CH_3O + H \rightarrow CH_4 + OH \quad (18)$$

3.2.1. Photocatalytic mechanism

To understand the photocatalytic mechanism of semiconductor-based photocatalysts, it is essential to determine their energy-band potentials since the redox ability of photogenerated carriers is associated with the energy-band potentials of photocatalysts. XPS valence band and UPS spectroscopy measurements were carried out to investigate the band structures of the samples. Fig. S7 shows the valence band maxima (VBM) for the pristine STO (1.88 eV) and NDs (1.25 eV), which were obtained by linearly extrapolating the low binding energy edge intersecting with the XPS background. Knowing the relationship between the vacuum energy (E_{abs}) and the normal electrode potential (E) (i.e., $E_{abs} = -E - 4.44$ [58]), and the work function of the XPS instrument (i.e., 5.7 eV), we calculated the VBM positions of STO and NDs to be 3.14 eV and 2.51 eV, respectively. Therefore, the respective conduction band minima (CBM) of STO and NDs were determined to be −0.14 eV and −0.37 eV according to the optical band gap. A plausible photocatalytic mechanism of CO_2 hydrogenation with the as-optimized STO-ND-Ru composite is schematically shown in Fig. 5. Upon light irradiation (1), both STO and ND generate photoinduced species, where the electrons are excited to the CB, thus creating electron–hole pairs. It is worth noting that the ND, which is also a potential semiconductor, can easily associate with STO in the form of a heterojunction. (2) Some excited electrons in STO with a lower CBM can recombine with the holes in NDs with a higher VBM. This is an important step in the charge transfer pathways of the heterojunction. (3) The photoexcited electrons accumulate in the CBM of the NDs and migrate to the lower CBM of STO and neighbouring Ru metal ions, retaining more reactive excited electrons and holes in the VBM of the STO and NDs. Also, the electron density increases on the CBM of STO [59]. Thus, the recombination of electron–hole pairs can be effectively suppressed in the composites, which leads to increased availability of carriers for photocatalytic reactions. (4) Thus, these electron-rich Ru metal ions can efficiently reduce CO_2. On the other hand, the VB potential of STO is more positive than the VB potential of NDs, indicating that the photogenerated h^+ can react with adsorbed H_2O to produce hydroxyl radicals as shown in Eqs. 11 and 12 [60–62].

4. Conclusions

In summary, the sequential deposition of noble metals and NDs on STO surface was achieved via wet impregnation method. The light absorption properties of the STO-X, STO-X-ND, and STO-ND-X composites were influenced. When the noble metals are deposited at the STO surface, the band gap was influenced slightly, while following the deposition of NDs, a decreasing trend of the band gap energy was observed. Also, specific surface areas of the STO-X-ND and STO-ND-X samples were increased with the deposition of NDs. The selective deposition also directly affected the formation and selectivity of the products, i.e., ND directly attached to STO enhanced the formation of CH_4. However, the samples containing noble metals produced mostly CO and small amounts of CH_4. DRIFTS study revealed formate (*$HCOO^-$) as the key intermediate in the formation of CO and CH_4 during the reaction mechanism for STO-ND-X and STO-X-ND composites, however, for pristine STO carboxyl (*COOH) was observed to be the main intermediate.

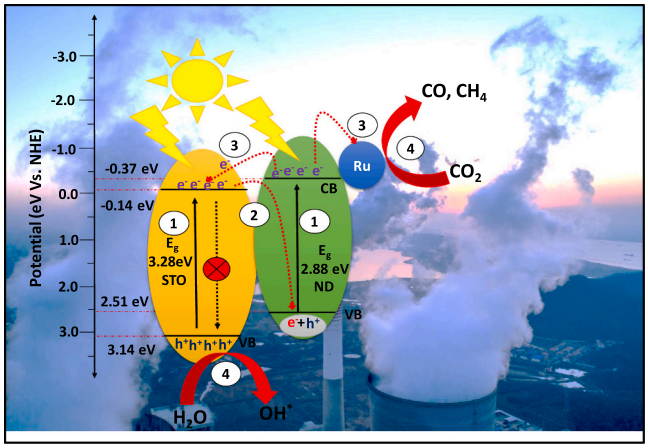

Fig. 5. Proposed mechanism for the photocatalytic hydrogenation of CO_2 upon the STO-ND-Ru composite.

CRediT authorship contribution statement

Mohit Yadav, first author, Conceptualization, Investigation, Writing - Original Draft, Data Curation, Methodology, Visualization, Tamás Gyulavári, co-author, Investigation, Data Curation, Writing – review & editing, Janos Kiss, co-author, Investigation, Kornélia B. Ábrahámné, co-author, Investigation, Anastasiia Efremova, co-author, Investigation, Ákos Szamosvölgyi, co-author, Investigation, Zsolt Pap corresponding author, Conceptualization, Methodology, Resources, Visualization, Supervision, Project administration, Writing – review & editing, Funding acquisition, András Sápi, corresponding author, Conceptualization, Resources, Supervision, Project administration, Funding acquisition, Ákos Kukovecz, co-author, Resources, Funding acquisition, Zoltán Kónya, co-author, Resources, Funding acquisition.

Declaration of Competing Interest

The authors declare that they have no known competing financial interests or personal relationships that could have appeared to influence the work reported in this paper.

Data availability

Data will be made available on request.

Acknowledgements

AS gratefully acknowledges the support of the Bolyai Janos Research Fellowship of the Hungarian Academy of Science and the " ÚNKP-22–5 -SZTE-587" New National Excellence Program as well as the funding provided by the Indo-Hungarian TÉT project (2019–2.1.13-TÉT_IN-2020–00015) and FK 143583 of NKFIH and Project no. TKP2021-NVA-19 under the TKP2021-NVA funding scheme of the Ministry for Innovation and Technology and ZK is grateful for K_21 138714 and SNN_135918 project from the source of the National Research, Development and Innovation Fund. The Ministry of Human Capacities

through the EFOP-3.6.1–16-2016–00014 project and the 20391–3/2018/FEKUSTRAT are acknowledged. Project no. RRF-2.3.1–21-2022–00009, titled National Laboratory for Renewable Energy has been implemented with the support provided by the Recovery and Resilience Facility of the European Union within the framework of Programme Széchenyi Plan Plus. T. Gyulavári is grateful for the financial support of the NKFI-PD-138248 project, the Bolyai János scholarship provided by the Hungarian Academy of Sciences, and that the research was supported by the ÚNKP-23–4 New National Excellence Program of the Ministry for Culture and Innovation from the source of the National Research, Development and Innovation Fund.

Appendix A. Supporting information

Supplementary data associated with this article can be found in the online version at doi:10.1016/j.jcou.2023.102621.

References

[1] D.T. Whipple, P.J. Kenis, Prospects of CO_2 utilization via direct heterogeneous electrochemical reduction, J. Phys. Chem. Lett. 1 (2010) 3451–3458.
[2] B. Kumar, J.P. Brian, V. Atla, S. Kumari, K.A. Bertram, R.T. White, J.M. Spurgeon, New trends in the development of heterogeneous catalysts for electrochemical CO_2 reduction, Catal. Today 270 (2016) 19–30.
[3] A. Roldan, N. Hollingsworth, A. Roffey, H.-U. Islam, J. Goodall, C. Catlow, J. Darr, W. Bras, G. Sankar, K. Holt, Bio-inspired CO 2 conversion by iron sulfide catalysts under sustainable conditions, Chem. Commun. 51 (2015) 7501–7504.
[4] J. Ma, N. Sun, X. Zhang, N. Zhao, F. Xiao, W. Wei, Y. Sun, A short review of catalysis for CO_2 conversion, Catal. Today 148 (2009) 221–231.
[5] M.K. Gnanamani, G. Jacobs, H.H. Hamdeh, W.D. Shafer, F. Liu, S.D. Hopps, G. A. Thomas, B.H. Davis, Hydrogenation of carbon dioxide over Co–Fe bimetallic catalysts, Acs Catal. 6 (2016) 913–927.
[6] X. Liu, C. Kunkel, P. Ramirez de la Piscina, N. Homs, F. Vines, F. Illas, Effective and highly selective CO generation from CO_2 using a polycrystalline α-Mo2C catalyst, ACS Catal. 7 (2017) 4323–4335.
[7] S. Zeng, P. Kar, U.K. Thakur, K. Shankar, A review on photocatalytic CO_2 reduction using perovskite oxide nanomaterials, Nanotechnology 29 (2018), 052001.
[8] X. Chang, T. Wang, J. Gong, CO 2 photo-reduction: insights into CO 2 activation and reaction on surfaces of photocatalysts, Energy Environ. Sci. 9 (2016) 2177–2196.
[9] V.-H. Nguyen, B.-S. Nguyen, Z. Jin, M. Shokouhimehr, H.W. Jang, C. Hu, P. Singh, P. Raizada, W. Peng, S.S. Lam, Towards artificial photosynthesis: Sustainable hydrogen utilization for photocatalytic reduction of CO_2 to high-value renewable fuels, Chem. Eng. J. 402 (2020), 126184.
[10] Z. Chen, Y. Hu, J. Wang, Q. Shen, Y. Zhang, C. Ding, Y. Bai, G. Jiang, Z. Li, N. Gaponik, Boosting photocatalytic CO_2 reduction on CsPbBr3 perovskite nanocrystals by immobilizing metal complexes, Chem. Mater. 32 (2020) 1517–1525.
[11] R. Shi, G.I. Waterhouse, T. Zhang, Recent progress in photocatalytic CO_2 reduction over perovskite oxides, Sol. Rrl 1 (2017) 1700126.
[12] H. Zhou, J. Guo, P. Li, T. Fan, D. Zhang, J. Ye, Leaf-architectured 3D hierarchical artificial photosynthetic system of perovskite titanates towards CO 2 photoreduction into hydrocarbon fuels, Sci. Rep. 3 (2013) 1–9.
[13] H. Yoshida, L. Zhang, M. Sato, T. Morikawa, T. Kajino, T. Sekito, S. Matsumoto, H. Hirata, Calcium titanate photocatalyst prepared by a flux method for reduction of carbon dioxide with water, Catal. Today 251 (2015) 132–139.
[14] U. Terranova, F. Vines, N.H. De Leeuw, F. Illas, Mechanisms of carbon dioxide reduction on strontium titanate perovskites, J. Mater. Chem. A 8 (2020) 9392–9398.
[15] B.L. Phoon, C.W. Lai, J.C. Juan, P.L. Show, W.H. Chen, A review of synthesis and morphology of SrTiO 3 for energy and other applications, Int. J. Energy Res. 43 (2019) 5151–5174.
[16] M.F. Ehsan, M.N. Ashiq, F. Bi, Y. Bi, S. Palanisamy, T. He, Preparation and characterization of SrTiO 3–ZnTe nanocomposites for the visible-light photoconversion of carbon dioxide to methane, RSC Adv. 4 (2014) 48411–48418.
[17] K. Xie, N. Umezawa, N. Zhang, P. Reunchan, Y. Zhang, J. Ye, Self-doped SrTiO 3− δ photocatalyst with enhanced activity for artificial photosynthesis under visible light, Energy Environ. Sci. 4 (2011) 4211–4219.
[18] V. Kumar, S. Choudhary, V. Malik, R. Nagarajan, A. Kandasami, A. Subramanian, Enhancement in photocatalytic activity of SrTiO3 by tailoring particle size and defects, physica status solidi (a), 216 (2019) 1900294.
[19] W. Chen, L. Chang, S.-B. Ren, Z.-C. He, G.-B. Huang, X.-H. Liu, Direct Z-scheme 1D/2D WO2. 72/ZnIn2S4 hybrid photocatalysts with highly-efficient visible-light-driven photodegradation towards tetracycline hydrochloride removal, J. Hazard. Mater. 384 (2020), 121308.
[20] G. Drera, A. Giampietri, A. Febbrari, M. Patrini, M.C. Mozzati, L. Sangaletti, Band offset and gap tuning of tetragonal CuO− SrTiO 3 heterojunctions, Phys. Rev. B 99 (2019), 075124.
[21] Y. Jin, D. Jiang, D. Li, P. Xiao, X. Ma, M. Chen, SrTiO3 nanoparticle/SnNb2O6 nanosheet 0D/2D heterojunctions with enhanced interfacial charge separation and photocatalytic hydrogen evolution activity, ACS Sustain. Chem. Eng. 5 (2017) 9749–9757.
[22] Y.-Y. Pai, A. Tylan-Tyler, P. Irvin, J. Levy, Physics of SrTiO3-based heterostructures and nanostructures: a review, Rep. Prog. Phys. 81 (2018), 036503.
[23] D. Li, S. Ouyang, H. Xu, D. Lu, M. Zhao, X. Zhang, J. Ye, Synergistic effect of Au and Rh on SrTiO 3 in significantly promoting visible-light-driven syngas production from CO 2 and H 2 O, Chem. Commun. 52 (2016) 5989–5992.
[24] A. Tanaka, Y. Nishino, S. Sakaguchi, T. Yoshikawa, K. Imamura, K. Hashimoto, H. Kominami, Functionalization of a plasmonic Au/TiO 2 photocatalyst with an Ag co-catalyst for quantitative reduction of nitrobenzene to aniline in 2-propanol suspensions under irradiation of visible light, Chem. Commun. 49 (2013) 2551–2553.
[25] W. Tu, Y. Zhou, H. Li, P. Li, Z. Zou, Au@ TiO 2 yolk–shell hollow spheres for plasmon-induced photocatalytic reduction of CO 2 to solar fuel via a local electromagnetic field, Nanoscale 7 (2015) 14232–14236.
[26] V.N. Mochalin, O. Shenderova, D. Ho, Y. Gogotsi, The properties and applications of nanodiamonds, Nat. Nanotechnol. 7 (2012) 11–23.
[27] D. Mateo, J. Albero, H. Garcia, Titanium-perovskite-supported RuO2 nanoparticles for photocatalytic CO_2 methanation, Joule 3 (2019) 1949–1962.
[28] M. Qureshi, A.T. Garcia-Esparza, G. Jeantelot, S. Ould-Chikh, A. Aguilar-Tapia, J.-L. Hazemann, J.-M. Basset, D. Loffreda, T. Le Bahers, K. Takanabe, Catalytic consequences of ultrafine Pt clusters supported on SrTiO3 for photocatalytic overall water splitting, J. Catal. 376 (2019) 180–190.
[29] Q. Wu, J. Cen, K.R. Goodman, M.G. White, G. Ramakrishnan, A. Orlov, Understanding the interactions of CO_2 with doped and undoped SrTiO3, ChemSusChem 9 (2016) 1889–1897.
[30] S. Shoji, X. Peng, A. Yamaguchi, R. Watanabe, C. Fukuhara, Y. Cho, T. Yamamoto, S. Matsumura, M.-W. Yu, S. Ishii, Photocatalytic uphill conversion of natural gas beyond the limitation of thermal reaction systems, Nat. Catal. 3 (2020) 148–153.
[31] L.M. Pastrana-Martinez, S. Morales-Torres, S.A. Carabineiro, J.G. Buijnsters, J. L. Faria, J.L. Figueiredo, A.M. Silva, Nanodiamond-TiO^ sub 2^ composites for heterogeneous photocatalysis, ChemPlusChem 78 (2013) 801.
[32] J. Liu, P. Wang, W. Qu, H. Li, L. Shi, D. Zhang, Nanodiamond-decorated ZnO catalysts with enhanced photocorrosion-resistance for photocatalytic degradation of gaseous toluene, Appl. Catal. B: Environ. 257 (2019), 117880.
[33] Z. Lin, J. Xiao, L. Li, P. Liu, C. Wang, G. Yang, Nanodiamond-embedded p-type copper (I) oxide nanocrystals for broad-spectrum photocatalytic hydrogen evolution, Adv. Energy Mater. 6 (2016) 1501865.
[34] D. Jiang, X. Sun, X. Wu, L. Shi, F. Du, Hydrothermal synthesis of single-crystal Cr-doped SrTiO3 for efficient visible-light responsive photocatalytic hydrogen evolution, Mater. Res. Express 7 (2020), 015047.
[35] Y. Wang, J. Ren, K. Deng, L. Gui, Y. Tang, Preparation of tractable platinum, rhodium, and ruthenium nanoclusters with small particle size in organic media, Chem. Mater. 12 (2000) 1622–1627.
[36] É. Karácsonyi, L. Baia, A. Dombi, V. Danciu, K. Mogyorósi, L. Pop, G. Kovács, V. Coşoveanu, A. Vulpoi, S. Simon, The photocatalytic activity of TiO2/WO3/noble metal (Au or Pt) nanoarchitectures obtained by selective photodeposition, Catal. Today 208 (2013) 19–27.
[37] D. Chapron, F. Cordero, M.D. Fontana, Characterization of oxygen vacancies in SrTiO3 by means of anelastic and Raman spectroscopy, J. Appl. Phys. 126 (2019), 154101.
[38] Z. Bao, V. Fung, J. Moon, Z.D. Hood, M. Rochow, J. Kammert, F. Polo-Garzon, Z. Wu, Revealing the interplay between “intelligent behavior” and surface reconstruction of non-precious metal doped SrTiO3 catalysts during methane combustion, Catal. Today (2022).
[39] Z. Zhang, P. Qian, X. Yang, B. Wu, H. Cai, F. Zhang, X. Wu, Manipulating the carrier concentration and phase transition via Nb content in SrTiO3, Sci. Rep. 12 (2022) 1–7.
[40] A. Biswas, S. Paul, A. Banerjee, Carbon nanodots, Ru nanodots and hybrid nanodots: preparation and catalytic properties, J. Mater. Chem. A 3 (2015) 15074–15081.
[41] C. Wang, S. Fang, S. Xie, Y. Zheng, Y.H. Hu, Thermo-photo catalytic CO 2 hydrogenation over Ru/TiO 2, J. Mater. Chem. A 8 (2020) 7390–7394.
[42] R. Chong, C. Su, Z. Wang, Z. Chang, L. Zhang, D. Li, Enhanced Photocatalytic Reduction of CO 2 on Rutile TiO 2/MgAl Layered Double Oxides with H 2 O Under Ambient Temperature, Catal. Lett. 150 (2020) 1061–1071.
[43] T. Gyulavári, D. Dusnoki, V. Márta, M. Yadav, M. Abedi, A. Sápi, Á. Kukovecz, Z. Kónya, Z. Pap, Dependence of photocatalytic activity on the morphology of strontium titanates, Catalysts 12 (2022) 523.
[44] S. Shoji, A. Yamaguchi, E. Sakai, M. Miyauchi, Strontium titanate based artificial leaf loaded with reduction and oxidation cocatalysts for selective CO_2 reduction using water as an electron donor, ACS Appl. Mater. Interfaces 9 (2017) 20613–20619.
[45] T. Ohashi, Y. Miyoshi, K. Katagiri, K. Inumaru, Photocatalytic reduction of carbon dioxide by strontium titanate nanocube-dispersed mesoporous silica, J. Asian Ceram. Soc. 5 (2017) 255–260.
[46] H. Sun, C. Dong, A. Huang, H. Zhan, G. Wang, W. Liu, B. Ma, W. Wang, Transition metal doping induces Ti3+ to promote the performance of SrTiO3@ TiO2 visible light photocatalytic reduction of CO_2 to prepare C1 product, Chem. Eur. J. 28 (2022), e202200019.
[47] H. Wei, J. Cai, Y. Zhang, X. Zhang, E.A. Baranova, J. Cui, Y. Wang, X. Shu, Y. Qin, J. Liu, Synthesis of SrTiO 3 submicron cubes with simultaneous and competitive photocatalytic activity for H 2 O splitting and CO 2 reduction, RSC Adv. 10 (2020) 42619–42627.

[48] B. Boga, N. Steinfeldt, N.G. Moustakas, T. Peppel, H. Lund, J. Rabeah, Z. Pap, V.-M. Cristea, J. Strunk, Role of SrCO3 on photocatalytic performance of SrTiO3-SrCO3 composites, Catalysts 12 (2022) 978.
[49] J.C. Wu, C.-W. Huang, In situ DRIFTS study of photocatalytic CO 2 reduction under UV irradiation, Front. Chem. Eng. China 4 (2010) 120–126.
[50] T. Rajkumar, A. Sápi, M. Ábel, J. Kiss, I. Szenti, K. Baán, J.F. Gómez-Pérez, Á. Kukovecz, Z. Kónya, Surface engineering of CeO2 catalysts: Differences between solid solution based and interfacially designed Ce1− xMxO2 and MO/CeO2 (M= Zn, Mn) in CO_2 hydrogenation reaction, Catal. Lett. 151 (2021) 3477–3491.
[51] J. Kiss, F. Solymosi, The effect of adsorbed oxygen on the stability of NCO on Rh (111) studied by reflection absorption infrared spectroscopy, J. Catal. 179 (1998) 277–282.
[52] S. Kattel, P. Liu, J.G. Chen, Tuning selectivity of CO_2 hydrogenation reactions at the metal/oxide interface, J. Am. Chem. Soc. 139 (2017) 9739–9754.
[53] Y. Guo, S. Mei, K. Yuan, D.-J. Wang, H.-C. Liu, C.-H. Yan, Y.-W. Zhang, Low-temperature CO_2 methanation over CeO2-supported Ru single atoms, nanoclusters, and nanoparticles competitively tuned by strong metal–support interactions and H-spillover effect, Acs Catal. 8 (2018) 6203–6215.
[54] B. László, K. Baán, E. Varga, A. Oszkó, A. Erdőhelyi, Z. Kónya, J. Kiss, Photo-induced reactions in the CO_2-methane system on titanate nanotubes modified with Au and Rh nanoparticles, Appl. Catal. B: Environ. 199 (2016) 473–484.
[55] A. Efremova, T. Rajkumar, A. Szamosvolgyi, A. Sapi, K. Baan, I. Szenti, J. Gomez-Perez, G. Varga, J. Kiss, G. Halasi, Complexity of a Co3O4 system under ambient-pressure CO_2 methanation: influence of bulk and surface properties on the catalytic performance, J. Phys. Chem. C. 125 (2021) 7130–7141.
[56] J. Wu, C.-W. Huang, In situ DRIFTS study of photocatalytic CO_2 reduction under UV irradiation, Front. Chem. Eng. China 4 (2010) 120–126.
[57] X.-L. Zhou, Z.-M. Liu, J. Kiss, D. Sloan, J. White, Surface chemistry of chloroiodomethane, coadsorbed with H and O, on Pt (111), J. Am. Chem. Soc. 117 (1995) 3565–3592.
[58] J.-C. Wang, L. Zhang, W.-X. Fang, J. Ren, Y.-Y. Li, H.-C. Yao, J.-S. Wang, Z.-J. Li, Enhanced photoreduction CO_2 activity over direct Z-scheme α-Fe2O3/Cu2O heterostructures under visible light irradiation, ACS Appl. Mater. Interfaces 7 (2015) 8631–8639.
[59] L. Zhang, J. Zhang, H. Yu, J. Yu, Emerging S-scheme photocatalyst, Adv. Mater. 34 (2022) 2107668.
[60] Z. Yu, K. Yang, C. Yu, K. Lu, W. Huang, L. Xu, L. Zou, S. Wang, Z. Chen, J. Hu, Steering unit cell dipole and internal electric field by highly dispersed Er atoms embedded into NiO for efficient CO_2 photoreduction, Adv. Funct. Mater. 32 (2022) 2111999.
[61] J. Zeng, L. Xu, X. Luo, T. Chen, S.-H. Tang, X. Huang, L.-L. Wang, Z-scheme systems of ASi 2 N 4 (A= Mo or W) for photocatalytic water splitting and nanogenerators, Tungsten (2022) 1–8.
[62] C. Xu, Q. Zhou, W.-Y. Huang, K. Yang, Y.-C. Zhang, T.-X. Liang, Z.-Q. Liu, Constructing Z-scheme β-Bi2O3/ZrO2 heterojunctions with 3D mesoporous SiO2 nanospheres for efficient antibiotic remediation via synergistic adsorption and photocatalysis, Rare Met. 41 (2022) 2094–2107.